DUST DESTRUCTION IN FAST SHOCKS OF CORE-COLLAPSE SUPERNOVA REMNANTS IN THE LARGE MAGELLANIC CLOUD

Brian J. Williams,[1] Kazimierz J. Borkowski,[1] Stephen P. Reynolds,[1] William P. Blair,[2] Parviz Ghavamian,[2]
Sean P. Hendrick,[3] Knox S. Long,[4] Sean Points,[5] John C. Raymond,[6] Ravi Sankrit,[2,7]
R. Chris Smith,[5] and P. Frank Winkler[8]

ABSTRACT

We report observations with the Multiband Imaging Photometer for *Spitzer* of four supernova remnants (SNRs) believed to be the result of core-collapse supernovae: N132D (0525–69.6), N49B (0525–66.0), N23 (0506–68.0), and 0453–68.5. All four of these SNRs were detected in whole at 24 μm and in part at 70 μm. Comparisons with *Chandra* broadband X-ray images show an association of infrared (IR) emission with the blast wave. We attribute the observed IR emission to dust that has been collisionally heated by electrons and ions in the hot, X-ray–emitting plasma, with grain size distributions appropriate for the LMC and the destruction of small grains via sputtering by ions. As with our earlier analysis of Type Ia SNRs, models can reproduce observed 70 μm/ 24 μm flux ratios only if effects from sputtering are included, destroying small grains. We calculate the mass of dust swept up by the blast wave in these remnants, and we derive a dust-to-gas mass ratio of several times less than the often assumed value of 0.25% for the LMC. We believe that one explanation for this discrepancy could be porous (fluffy) dust grains.

Subject headings: dust, extinction — Magellanic Clouds — supernova remnants

1. INTRODUCTION

Dust plays an important role in all stages of galaxy evolution. The life cycle of dust grains and the amount and relative abundances present in the interstellar medium (ISM) are determined by the balance between dust formation, grain modification, and dust destruction (Draine 2003). Dust destruction is known to occur in both fast and slow shocks in supernova remnants (SNRs; Jones 2004). We focus here on dust destruction via sputtering by high-energy ions in fast (nonradiative) shocks in SNRs.

SNRs make excellent probes of the dust content of the diffuse ISM in galaxies, since their shock waves create X-ray plasmas that heat dust in their vicinities. Ambient dust heated by starlight may escape detection, but shock-heated dust radiates strongly in *Spitzer* wavelengths, so SNR studies probe different conditions than studies of diffuse ISM dust emission. Modeling of X-ray emission provides the basis for understanding dust emission. Inferences of dust content and properties from SNR observations are thus complementary to UV-absorption studies, which rely on the fortuitous locations of background UV-bright stars (Jenkins et al. 1984). The combination of these types of investigation may lead to significant advances in our understanding of dust properties, with potential repercussions for gas-phase abundance determinations, theories of chemical evolution of galaxies, and dust-catalyzed cosmochemistry.

To examine the nature of dust heating and destruction in the ISM, we conducted an imaging survey with *Spitzer* of 39 SNRs in the Magellanic Clouds. In a previous paper (Borkowski et al. 2006, hereafter Paper I) we analyzed IR emission from SNRs resulting from Type Ia supernovae (SNe). We found that the dust-to-gas mass ratio was lower than the expected value of 0.25% (Weingartner & Draine 2001, hereafter WD01) for the surrounding ISM, a result that we attributed to Type Ia SNe exploding in lower density media. However, Tappe et al. (2006) found a low dust content in N132D, a remnant of a core-collapse SN that occurred in a dense ISM area, and suggested a high dust destruction efficiency in this SNR. A lower than expected dust content was also found in the circumstellar medium surrounding SN 1987A (Bouchet et al. 2006). In order to investigate this apparent dust deficit, we present here an analysis of four core-collapse SNRs, including N132D.

We base our inference of the core-collapse nature of our objects on the presence of a pulsar wind nebula in 0453–68.5 (Gaensler et al. 2003), a central compact object in N23 (Hayato et al. 2006; Hughes et al. 2006), the O-rich classification of N132D (Lasker 1978), and the presence of a large mass of Mg in N49B (Park et al. 2003).

All four of these remnants were detected in both the 24 and 70 μm bands of the Multiband Imaging Photometer for *Spitzer* (MIPS). We find a similar result to that found for the Type Ia remnants in Paper I: the dust-to-gas ratios we infer are lower by a factor of $\sim$4 than what is expected for the LMC. In § 4 we discuss possible reasons for this apparent dust deficiency.

2. OBSERVATIONS AND DATA REDUCTION

All four objects were observed with the 24 and 70 μm MIPS arrays. At 24 μm, we mapped each remnant in our survey and the surrounding background with 14 frames of 30.93 s each, for a total exposure time of 433 s. At 70 μm, we observed a total of 545 s in 52 frames for all but N132D, which we observed for 986 s in 94 frames. MIPS images were processed from Basic Calibrated Data (BCD) to post-BCD (PBCD) at the

[1] Physics Department, North Carolina State University, Raleigh, NC 27695-8202; bjwilli2@ncsu.edu.

[2] Department of Physics and Astronomy, Johns Hopkins, 3400 North Charles Street, Baltimore, MD 21218-2686.

[3] Physics Department, Millersville University, P.O. Box 1002, Millersville, PA 17551.

[4] Space Telescope Science Institute, 3700 San Martin Drive, Baltimore, MD 21218.

[5] National Optical Astronomy Observatory/Cerro Tololo Inter-American Observatory, Cailla 603, La Serena, Chile.

[6] Harvard-Smithsonian Center for Astrophysics, 60 Garden Street, Cambridge, MA 02138.

[7] Current address: University of California at Berkeley, Space Sciences Laboratory, 7 Gauss Way, Berkeley, CA 94720.

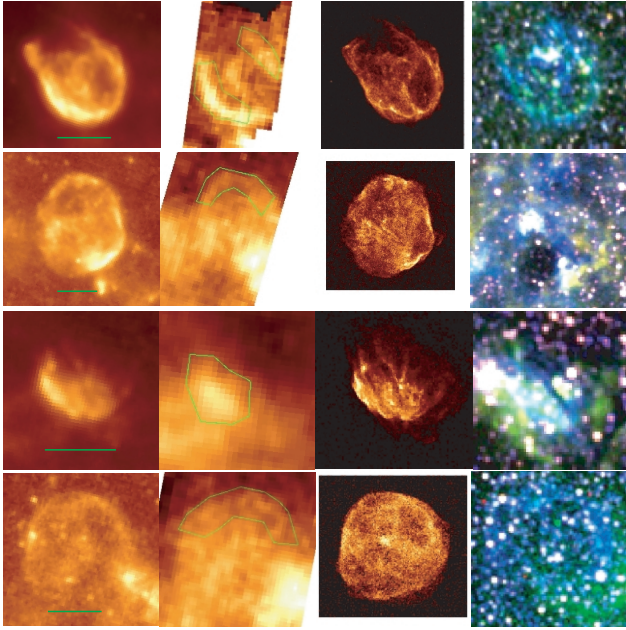[8] Department of Physics, Middlebury College, Middlebury, VT 05753.

Object	24 μm	70 μm	70 μm/24 μm
N132D NW	730 ± 73	430 ± 96	0.59 ± 0.13
N132 S	1000 ± 100	770 ± 170	0.76 ± 0.17
N49B	43 ± 4.3	395 ± 79	9.1 ± 2.0
0453–68.5	13 ± 1.3	250 ± 50	19 ± 4.2
N23	100 ± 10	240 ± 50	2.4 ± 0.5

NOTE.—All fluxes are given in units of millijanskys.

FIG. 1.—*Top row, from left to right*: N132D at 24 and 70 μm (the region of interest at 70 μm is marked on the image), in the X-rays (broadband, *Chandra* image) and in the optical (overlay of MCELS images, with [S II], Hα, and [O III] marked in red, green, and blue, respectively). Second, third, and fourth rows show the same sequence for N49B, N23, and 0453–68.5, respectively; 1′ scales are shown on the 24 μm images.

Spitzer Science Center (SSC) using version 13.2 of the PBCD pipeline. For the 70 μm images, we used the contributed software package GeRT to reprocess the raw telescope images into BCD images, then reprocessed the BCD images using the SSC software package MOPEX. GeRT was useful in removing some of the artifacts, such as vertical stripes, from the 70 μm data.

Figure 1 shows the 24 and 70 μm images as well as X-ray images from *Chandra* archival data and optical images from the Magellanic Cloud Emission-Line Survey (MCELS; Smith et al. 2005). Because line emission from low-ionization gases should be a significant contributor only in slower, radiative shocks, we conclude that we are seeing thermal IR emission primarily resulting from dust. Recent spectroscopic observations of N132D with *Spitzer* (Tappe et al. 2006) confirm that line contributions at 24 μm are negligible. Our measured fluxes are presented in Table 1.

3. MODELING

Because of the morphological similarities between the IR emission and the blast wave seen in X-rays, we believe that the dust present in the ISM is being collisionally heated by electrons and protons in the outward moving shock wave (Dwek & Arendt 1992). The modeling of dust emission for these remnants is similar to the modeling done on the four Type Ia remnants in Paper I, where it is described more fully. Our model uses a one-dimensional plane-shock approximation. The sputtering timescale, τ_p, is equal to $\int_0^t n_p \, dt$ and is one of the inputs to the code. The other inputs are electron temperature T_e, ion temperature T_i, gas density n, grain size distribution, and grain composition and relative abundances. For the composition, abundances, and distribution of dust grains, we follow WD01, particularly the model consisting of separate silicate and carbonaceous grain populations in fixed proportions, in a range of sizes from 1 nm to 1 μm. We use the "average" LMC

model with the maximum amount of small carbonaceous grains. We do not model emission features from polycyclic aromatic hydrocarbons, as these emission features are not expected to contribute in MIPS bands. In order to test the dependency of our results on the dust grain-size distribution, we also consider an alternative model put forth by Cartledge et al. (2005, hereafter C05). Dust masses derived from this model were nearly identical to those from the WD01 model, but since the C05 model predicts a higher dust-to-gas ratio in the LMC (0.45%), this model actually exaggerates the observed dust deficit. We thus report only the results from the WD01 model and believe that these results are conservative. X-ray analysis provides estimates of the electron temperature, ionization timescale $\tau_i \equiv \int_0^t n_e \, dt$, and emission measure EM $\equiv n_e M_g$ (M_g is mass of swept-up gas) of the plasma. We assume tight dust-gas coupling, since the gyro-radii of dust grains are small compared to the thickness of the shock (Dwek et al. 1996). We used archival *Chandra* data for our analysis and fit X-ray spectra using Sedov nonequilibrium ionization thermal models in XSPEC (Arnaud 1996; Borkowski et al. 2001). Emission-measure averaged T_e and T_i from these models and the reduced τ_i ($\frac{1}{3}$ of the Sedov τ_{ised}, defined as the product of the postshock electron density and the SNR age) were then used as inputs to our plane shock model. (The approximate factor $\frac{1}{3}$ arises from applying results of a spherical model to plane-shock calculations; see Fig. 4 of Borkowski et al. 2001). Since the T_i/T_e ratio is close to 1 in these models, we set $T_i = T_e$.

We employed two methods to model dust emission. In the first, we fix τ_p, T_e, and T_i as derived from X-rays (taking $\tau_p = \tau_i/1.2$), leaving only the density and total dust mass as free parameters. In the second, we use the dynamical age of the remnant, as derived from optical or global X-ray studies, leaving the shock age and density as free, but correlated, parameters. We find that these two different methods produce very similar results, within a factor of ~25%. We thus report only the inputs and results from the first method. Model input parameters are given in Table 2. The density of the gas is then adjusted to reproduce the observed 70 μm/24 μm flux ratio, and the 24 μm flux is normalized to the observed value to provide a total dust mass in the region of interest. The emission measure divided by the electron density gives an estimate for

Object	T_e (= T_i) (keV)	τ_p (10^3 cm^{-3} yr)	Age (yr)
N132D NW	0.61	17	2500[a]
N132D S	1.02	3.2	2500
N49B	0.36	2.4	10900[b]
0453–68.5	0.29	8.6	8700[b]
N23	0.56	6.7	4600[c]

[a] Morse et al. (1996).
[b] Gaensler et al. (2003).
[c] Hughes et al. (2006).

TABLE 3
MODEL RESULTS

Object (1)	n_p (cm^{-3}) (2)	T_{dust} (K) (3)	Dust Mass ($M_\odot$) (4)	$n_e M_g$ (cm^{-3} $M_\odot$) (5)	Dust/Gas (6)	Percent Destroyed (7)	Dust/Gas (Orig.) (8)	L_{36} (9)
N132D NW	34	95–120	0.0075	660	4.6×10^{-4}	50	9.2×10^{-4}	35
N132D S	14	85–105	0.015	1020	2.5×10^{-4}	38	4.0×10^{-4}	94
N49B	1.1	50–60	0.08	580	1.8×10^{-4}	27	2.4×10^{-4}	8.4
0453–68.5	0.63	40–55	0.10	120	6.1×10^{-4}	33	9.8×10^{-4}	4.5
N23	5.8	70–85	0.011	250	3.0×10^{-4}	39	4.9×10^{-4}	8.7

NOTES.—Col. (2): Postshock proton density. Col. (3): For 0.02–0.1 μm grains. Col. (4): Mass of dust currently observed, after sputtering (postshock). Col. (6): Ratio of current dust mass to swept-up gas mass. Col. (7): Percentage of dust destroyed via sputtering. Col. (8): Inferred dust-to-gas mass ratio in preshock ISM. Col. (9): $L_{36} \equiv L_{IR}/10^{36}$ ergs s^{-1}.

the amount of gas swept up by the blast wave, and dividing the dust mass by the gas mass gives us a dust-to-gas mass ratio for the shocked ISM. Finally, dust temperatures are calculated in our model. Because we use a range of grain sizes, we report a range of temperatures, since grains of different sizes will be heated differently under the same plasma conditions. The range of temperatures quoted is therefore the result of a single fit to the flux ratio. Results are summarized in Table 3.

3.1. N132D

SNR N132D has been well studied in optical wavelengths (Morse et al. 1996) and is one of the brightest remnants in the Magellanic Clouds at X-ray wavelengths. The remnant is extraordinarily bright at 24 μm, where we find a total flux of ~3 Jy, consistent with Tappe et al. (2006). It is the only remnant in our sample that is brighter at 24 μm than at 70 μm. This implies warm dust, and therefore a dense environment (to provide the inferred heating), consistent with the remnant being very bright in X-rays. Morse et al. (1996) estimate a preshock hydrogen density for this remnant of 3 cm^{-3} based on modeling of the photoionized shock precursor. We analyzed the northwest rim and the bright southern rim separately. We find high densities, in good agreement with the expected postshock proton density n_p of 12 cm^{-3}. Densities are higher by a factor of ~2 in the northwest, and comparatively less mass in gas in that region. The mass in dust, however, was comparable to what was found in the south, adjusting for the different sizes of the regions.

3.2. N49B

N49B is believed to be older than N132D, perhaps as old as 10,000 yr. The ionization age is lower than this, however, perhaps due to an explosion into a preexisting cavity (Hughes et al. 1998). This remnant is much fainter than N132D at all wavelengths, but especially so at 24 μm, and the flux ratio is lower by more than order of magnitude in N49B compared to N132D. This can be explained by the much lower density we find in N49B: $n_p = 1.1$ cm^{-3} from our dust models, and $n_p = 2.1$ cm^{-3} from a Sedov analysis of X-ray data. Since dust heating rates are strongly dependent on density, a low-density environment will result in much cooler dust, whose spectrum peaks at longer wavelengths. Despite the contrasts in density and flux ratio of more than an order of magnitude, the dust-to-gas ratio in this remnant is only 2 times lower than that found in N132D.

3.3. N23

At 70 μm, the brightest parts of the shell of N23 are clearly visible. The region selected for analysis completely enclosed the emission visible at 70 μm, which contained about 75% of

the emission visible at 24 μm. Dust modeling yields $n_p = 5.8$ cm^{-3}. Hughes et al. (2006) found densities of 10 and 23 cm^{-3} in a couple of X-ray–bright shocks in this region of the remnant.

3.4. 0453–68.5

Although 0453–68.5 had the highest 70 μm/24 μm ratio of any remnant in this sample, only the north rim of the shell was clearly separable from the background at 70 μm. This is due to the overall faintness of the remnant, the high levels of background in the region, and the lower sensitivity of the 70 μm array. Nonetheless, there was sufficient signal-to-noise ratio to analyze the north rim of the remnant. The density found from modeling dust emission, $n_p = 0.63$ cm^{-3}, was also the lowest of these remnants. Sedov modeling of X-rays yielded a value of $n_p = 1.1$ cm^{-3}. Both the temperature and density are consistent with the observations of overall faintness at 24 μm and a high 70 μm/24 μm ratio.

4. DISCUSSION AND CONCLUSIONS

We find excellent (generally within a factor of 2) agreement between densities derived from dust modeling and estimated from optical and X-ray data. As has been proposed in the past (e.g., Dwek & Arendt 1992), dust emission is indeed a valuable density diagnostic of X-ray–emitting plasmas. The good match between X-ray and IR derived densities suggests that the X-ray–emitting gas is not highly clumped.

Our basic quantitative results are contained in Table 3. First, note that the total mass in dust we infer is quite small, of order 0.01–0.1 $M_\odot$, for all objects. Morphological evidence suggests that this dust is associated with the blast wave, but these values also serve as restrictive upper limits for the amount of ejecta dust that can have been produced in these core-collapse supernovae. They are, for the most part, less than the 0.08 $M_\odot \lesssim M_d \lesssim 0.3$ $M_\odot$ calculated by Todini & Ferrara (2001). Substantial amounts of dust can be destroyed when the ejecta are reverse-shocked, but the ejecta dust mass ultimately delivered to the ISM appears to be quite small. This is consistent with the findings of Stanimirovic et al. (2005), who analyzed IR emission from the LMC SNR 1E 0102.2−7219.

We find that, on average, about 40% of the mass in dust grains, including ~90% of the mass in grains smaller than 0.04 μm, has been destroyed via sputtering in these remnants. After accounting for this sputtering, we find an initial dust-to-gas ratio that is lower by a factor of roughly 4 than what is generally expected for the LMC. The values in Table 3 are similar to the dust-to-gas ratios we found in remnants from Type Ia SNe, and they are still well below the value reported in WD01 of ~2.5 × 10^{-3}. In Paper I we speculated that low dust-to-gas ratios might

be expected for Type Ia remnants expanding into lower-than-average density material, in which previous supernovae might have destroyed some grains. Since we now have a similar deficit for core-collapse remnants expanding into denser media, this explanation is less likely, although it is still possible that the dust content is generally low in the vicinity of core-collapse SNe.

The overall lower dust-to-gas ratios we infer will require another explanation. It is possible that sputtering timescales or rates might have been underestimated. Our models indicate that sputtering timescales would have to be increased by an order of magnitude, on average, to match the expected dust-to-gas ratio in the WD01 model, an unlikely possibility. Various factors could increase sputtering rates. Sputtering can be enhanced by increased relative velocities between ions and grains, either caused by grain motions (not included in our models) or by higher than assumed ion temperatures. In order to estimate the importance of such effects, we doubled ion temperatures in our shock models, resulting in only a 10%–15% increase in the fraction of the original dust destroyed for the relatively fast shocks considered here. Sputtering is expected to be enhanced for nonspherical grains with increased surface-to-volume ratio S/V. For a prolate ellipsoidal grain with an axial ratio of 2, S/V is twice as large as for a spherical grain, which enhances sputtering rates by a modest factor of 2. We find it unlikely that these modest enhancements in sputtering rates can account for the lower than expected dust-to-gas mass ratios.

Porous (fluffy) grains provide a possible explanation for the low dust-to-gas ratios. Porous grains (Mathis 1996) can be characterized by a porosity (fraction of grain volume devoid of material) $\mathcal{P}$. Such grains have an extinction per unit mass generally larger than for spherical compact grains. Voshchinnikov et al. (2006) modeled visual and UV absorption toward ζ Oph and σ Sco with a mixture of highly porous ($\mathcal{P} \gtrsim 0.9$) and compact grains with dust mass of only 70% and 44% of the dust mass in the WD01 model.

We expect enhanced sputtering rates for porous grains compared with spherical compact grains. A highly porous ($\mathcal{P} = 0.9$) grain has a surface area 4.6 times larger than a compact grain of the same mass, so for the same sputtering yields an

enhancement of sputtering rates by a factor of 4.6 is expected. In addition, protons, α-particles, and heavier ions can penetrate much deeper into porous grains, because their range within the solid is inversely proportional to the mean grain density. A proton with energy E will penetrate $0.09(E/1\ \mathrm{keV})$ μm into a porous silicate grain with $\mathcal{P} = 0.9$ (we used eq. [18] of Draine & Salpeter [1979] to estimate the proton projected range R_p). Jurac et al. (1998) found that sputtering yields are enhanced if the grain radius a is less than $3R_p$ because of additional sputtering from the back and sides of the grain. Grains as large as $0.25(E/1\ \mathrm{keV})$ μm are then destroyed more efficiently. It is also possible that the rough surface geometry expected for porous grains could result in a further enhancement of sputtering rates, as the protruding grain extensions comparable in size to the proton or α-particle projected ranges could be more readily sputtered (Jurac et al. 1998). An order of magnitude enhancement in sputtering rates is thus possible for highly porous grains.

The reduced preshock dust content and substantial enhancement in sputtering rates that result from porous grain models provide a promising explanation for the apparent dust deficit in LMC SNRs. These effects might be partially offset by the increased IR emissivity of porous grains (Voshchinnikov et al. 2006), as less dust is then required to account for the observed IR emission. It is possible, however, that compact grains dominate the observed IR emission, if porous grains (or porous mantles surrounding compact cores) have been preferentially destroyed. Modeling of *Spitzer* observations with porous grain models is required to assess whether these models can resolve the apparent dust deficit in LMC SNRs, including SNR 1987A. Spectroscopic follow-up on these remnants in the far-IR is required to confirm and strengthen our results. Implications of a resolution go beyond these particular SNRs or even the LMC as a whole and could help bring about a significant improvement in our understanding of interstellar dust in general.

REFERENCES

Arnaud, K. A. 1996, in ASP Conf. Ser. 101, Astronomical Data Analysis and Systems V, ed. G. Jacoby & J. Barnes (San Francisco: ASP), 17
Borkowski, K. J., Lyerly, W. J., & Reynolds, S. P. 2001, ApJ, 548, 820
Borkowski, K. J., et al. 2006, ApJ, 642, L141 (Paper I)
Bouchet, P., et al. 2006, ApJ, 650, 212
Cartledge, S. I. B., et al. 2005, ApJ, 630, 355 (C05)
Draine, B. T. 2003, ARA&A, 41, 241
Draine, B. T., & Salpeter, E. E. 1979, ApJ, 231, 77
Dwek, E., & Arendt, R. G. 1992, ARA&A, 30, 11
Dwek, E., Foster, S. M., & Vancura, O. 1996, ApJ, 457, 244
Gaensler, B. M., Hendrick, S. P., Reynolds, S. P., & Borkowski, K. J. 2003, ApJ, 594, L111
Hayato, A., Bamba, A., Tamagawa, T., & Kawabata, K. 2006, ApJ, in press
Hughes, J. P., Hayashi, I., & Koyama, K. 1998, ApJ, 505, 732
Hughes, J. P., et al. 2006, ApJ, 645, L117

Jenkins, E. B., Wallerstein, G. W., & Silk, J. 1984, ApJ, 278, 649
Jones, A. P. 2004, in ASP Conf. Ser. 309, Astrophysics of Dust, ed. A. N. Witt, C. C. Clayton, & B. T. Draine (San Francisco: ASP), 347
Jurac, S., Johnson, R. E., & Donn, B. 1998, ApJ, 503, 247
Lasker, B. M. 1978, ApJ, 223, 109
Mathis, J. S. 1996, ApJ, 472, 643
Morse, J. A., et al. 1996, AJ, 112, 509
Park, S., et al. 2003, ApJ, 592, L41
Smith, R. C., et al. 2005, BAAS, 37, 1200
Stanimirovic, S., et al. 2005, ApJ, 632, L103
Tappe, A., Rho, J., & Reach, W. T. 2006, ApJ, in press
Todini, P., & Ferrara, A. 2001, MNRAS, 325, 726
Voshchinnikov, N. V., Il'in, V. B., Henning, Th., & Dubkova, D. N. 2006, A&A, 445, 167
Weingartner, J. C., & Draine, B. T. 2001, ApJ, 548, 296 (WD01)